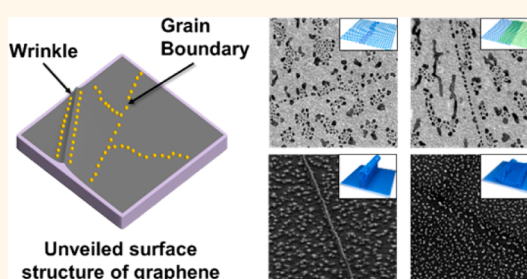# Simultaneous Visualization of Graphene Grain Boundaries and Wrinkles with Structural Information by Gold Deposition

Seong Uk Yu,[†,‡,⊥] Beomjin Park,[§,⊥] Yeonchoo Cho,[‡,⊥] Seung Hyun,[§] Jin Kon Kim,[§,*] and Kwang S. Kim[†,*]

[†]Department of Chemistry, Ulsan National Institute of Science and Technology (UNIST), Ulsan 689-798, Korea, and [‡]Department of Chemistry and [§]Department of Chemical Engineering, Pohang University of Science and Technology, Pohang 790-784, Korea. [⊥]S. U. Yu, B. Park, and Y. Cho contributed equally.

ABSTRACT Although line defects such as grain boundaries (GBs) and wrinkles are unavoidable in graphene, difficulties in identification preclude studying their impact on electronic and mechanical properties. As previous methods focus on a single type of line defect, simultaneous measurements of both GBs and wrinkles with detailed structural information have not been reported. Here, we introduce effective visualization of both line defects by controlled gold deposition. Upon depositing gold on graphene, single lines and double lines of gold nanoparticles (NPs) are formed along GBs and wrinkles, respectively. Moreover, it is possible to analyze whether a GB is stitched or overlapped, whether a wrinkle is standing or folded, and the width of the standing collapsed wrinkle. Theoretical calculations show that the characteristic morphology of gold NPs is due to distinct binding energies of line defects, which are correlated to disrupting diffusion of NPs. Our approach could be further exploited to investigate the defect structures of other two-dimensional materials.

Graphene produced from chemical vapor deposition (CVD) inevitably has defects that may alter its properties. Although CVD is the most promising technique for industrial-scale fabrication of graphene,[1−3] diverse defects are formed due to multiple seeds and differential thermal expansion coefficients.[4−7] Among these defects, line defects are of utmost importance, because even a single line defect can form two separated grains. The electrical and mechanical properties of graphene largely depend on line defects and grain sizes.[8−10] Generally, there are two types of line defects: wrinkles and grain boundaries (GBs). More specifically, there are two types of GBs: stitched and overlapped.[11] Wrinkles are also categorized into two types: standing collapsed wrinkle and folded wrinkle.[7] Table 1 illustrates the shape and the size of each defect.

The systematic study of line defects is still limited due in part to difficulties in visualization of these diverse surface structures.

More importantly, none of the methods can simultaneously visualize both GBs and wrinkles, despite recent advances in probing and identifying line defects.[4,10,12−16] GBs have mainly been studied using scanning tunneling microscopy (STM)[17] or dark-field tunneling electron microscopy (TEM).[4] These techniques give the structural information on GBs, but sample preparation is tricky and the spatial detection range is too narrow. On the other hand, oxidation of the copper substrate achieved visualization of GBs under optical microscopy.[12,13] However, this technique cannot identify the structure of line defects, and the GBs are not visible in the absence of the metal substrate. Wrinkles have mainly been studied using atomic force microscopy (AFM).[5,7] The problem is that the lateral resolution of AFM is generally not high enough for the analysis of very narrow wrinkles. Up to now, the width of a standing collapsed wrinkle has not been reported. Both types of defects are known to affect
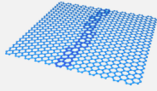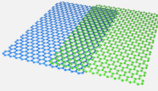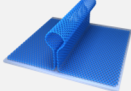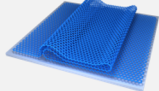
TABLE 1. Shapes of Stitched GB, Overlapped GB, Standing Collapsed Winkle, and Folded Wrinkle[a]

	Stitched GB	Overlapped GB	Standing Collapsed wrinkle	Folded wrinkle
Shape				
Width	3 ~ 4 Å	10 ~ 50 nm	~ 2 nm (first observed)	~ 100 nm
Height			2 ~ 6 nm	~1 nm

[a] The typical width and height of each defect are described.

electronic and mechanical properties of graphene. Thus, if one focuses on a single type of defect while ignoring the other, the interpretation of experimental results might lead to wrong information. Therefore, it is necessary to develop a method to visualize and identify the structure of GBs and wrinkles in a single observation.

Here we report a novel and very effective visualization method for both GBs and wrinkles simultaneously by gold deposition. Previously, gold deposition was used to identify the number of layers from mechanically exfoliated graphene. This is possible because the diffusion coefficient of gold depends on the number of layers.[18−20] Although the adhesive property of line defects[13] changes the graphene surface diffusion coefficient, this subtle difference is not significant enough to visualize line defects by simple gold deposition on graphene. Because the diffusion process highly depends on annealing conditions, this exploitation could lead to a substantial difference in identifying the line defects. The thermal energy control by tuning annealing conditions limits the diffusion of gold nanoparticles (NPs) on line defects. Using optimized gold deposition conditions, GBs and wrinkles were clearly and simultaneously visualized by using scanning electron microscopy (SEM), and the structures of these line defects were thoroughly characterized by TEM. First-principles calculations clearly explain the experimental data in terms of binding energy, which affects the diffusion coefficient as the key variable.

RESULTS AND DISCUSSION

To image defects, gold was slowly evaporated onto graphene on a SiO$_2$ substrate up to a thickness of 5 Å by using a thermal evaporator at 0.1 Å/s under a vacuum of $10^{−7}$ Torr (Figure 1a). The annealing process is performed simultaneously with evaporation of gold. Using Raman spectroscopy, we confirmed that the graphene used in this work was single-layer (Figure S1).

Figure 1b shows the SEM image of the graphene surface decorated with gold NPs without annealing.

No distinct features can be identified on the graphene surface structure, because gold diffusion does not take place to reveal the characteristics of the underlying surface. In contrast, Figure 1c shows the graphene surface decorated with gold NPs after 3 h of annealing at 300 °C. In this sample, the surface structures cannot be identified since most of the NPs are clustered together. This result implies that large particles are formed by agglomeration of the smaller mobile gold NPs at increased temperatures. More importantly, this behavior is observed even at defect sites because of too mobile gold particles at high temperature. Thus, the annealing conditions (temperature and time) should be carefully controlled to diffuse particles on the basal graphene plane. We found that the best condition for imaging is when gold is deposited on the substrate at 140 °C and then annealed at this temperature for an hour. When the mobility of gold NPs is carefully tuned by annealing, the morphology of gold NPs exposes diverse surface structures (Figure 1d).

A closer look at the SEM image reveals that gold NPs are aggregated along a single line or double lines on graphene. We claim that single and double lines of gold NPs are formed due to GBs and standing collapsed wrinkles, respectively. We will discuss folded wrinkles later. The red arrows indicate GBs, while the blue arrows indicate wrinkles. The particles in these lined structures are smaller than those in the basal graphene. This indicates the presence of sites that provide a larger binding energy difference, which disrupts diffusion of gold NPs. In CVD graphene the only structural line defects present are GBs and wrinkles. GBs are visualized as a single line of gold NPs because the GB is made of a line of defects such as five-membered and seven-membered rings or edges of graphene in the case of overlapped GBs, the chemical instability of which increases the binding energy with gold. Wrinkles are visualized as double lines because there are two sides in a wrinkle. The increased binding energy difference and the smaller sizes of gold NPs at
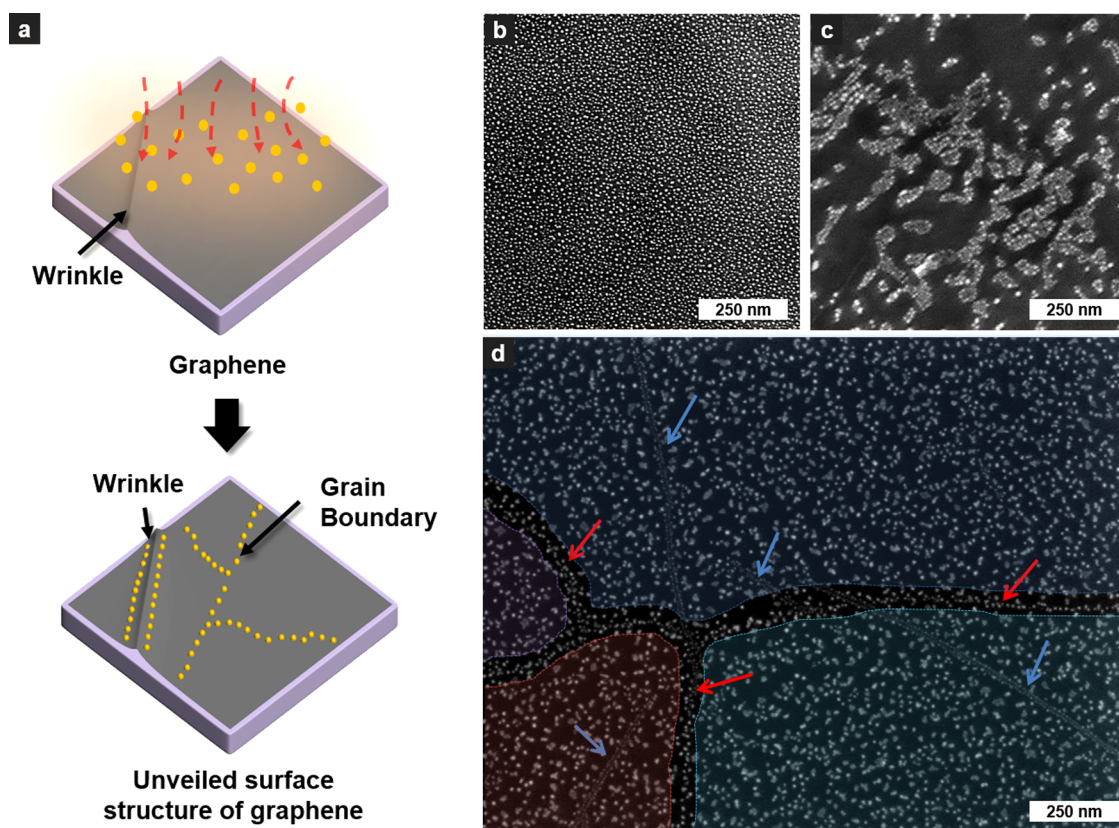
Figure 1. Observation of graphene grain boundaries and wrinkles after gold deposition. Schematic illustration of gold deposition on the graphene surface (a). SEM image of the graphene surface decorated by gold NPs without annealing (b), after 3 h of annealing at 300 °C (c), and after an hour of annealing at 140 °C (red arrows indicate GBs; blue arrows indicate wrinkles) (d).

wrinkles are attributed to (1) the increased sp^3 character of carbons arising from curvature and (2) the loss of van der Waals (vdW) stabilization by the detachment from the substrate. Using first-principles calculations we will show later that a gold adatom preferentially binds to these sites. Connectivity and waviness are additional indications that single and double lines of gold NPs correspond to GBs and wrinkles, respectively; a wrinkle is usually straight but sometimes disappears at a certain point (*i.e.*, not completely connected), while a GB is connected and wavy. Note that a GB and a wrinkle can cross each other (Figure 1d).

We confirm from TEM that a single line of gold NPs indicates the presence of a GB underneath. In addition, gold NPs also show whether a GB is stitched or overlapped. We observed the selective area electron diffraction (SAED) pattern across the GB lines from red to blue circle in two samples (Figure 2). Since the graphene lattice is rotated across the GB, grains can be identified from the rotation of the diffraction pattern. Each colored SAED pattern is obtained from the same colored area in the TEM image, representing a single grain. As the aperture moves across the gold NPs line, the hexagonal set of the SAED pattern was tilted in both cases. These results directly prove that gold NPs were agglomerated along GBs. A ring pattern for gold

NPs indicates that they have no preferred direction in growth, even when gold NPs are grown on the basal plane without defects. Furthermore, the stitched and overlapped GBs can be distinguished from gold deposition in the TEM image. The inset of each figure represents the corresponding structure of the GBs. Figure 2a shows that a stitched GB aligns gold NPs as a clear single line. This is expected because the width of stitched GBs is very narrow, being less than 10 Å.

On the other hand, Figure 2b strongly supports that another type of single line was formed along overlapped GBs; that is, one gold line is clear and continuous, but the other is not. This could be explained by the structure of overlapped GBs. Two edges are seen in the high-resolution TEM image (Figure S2). Since the edge of graphene is also the site providing a higher binding energy than the basal plane, gold NPs prefer to nucleate and grow near overlapped GBs. The lower edge of graphene cannot provide sufficient affinity to make the second line of gold NPs; however the morphology of gold NPs is so sensitive to the underlying surface that even a subtle difference such as a covered edge can be distinguished. They are distinguishable from the folded wrinkles in Figure S3.

We also successfully identified different types of wrinkles from the double lines of gold NPs (Figure 3).
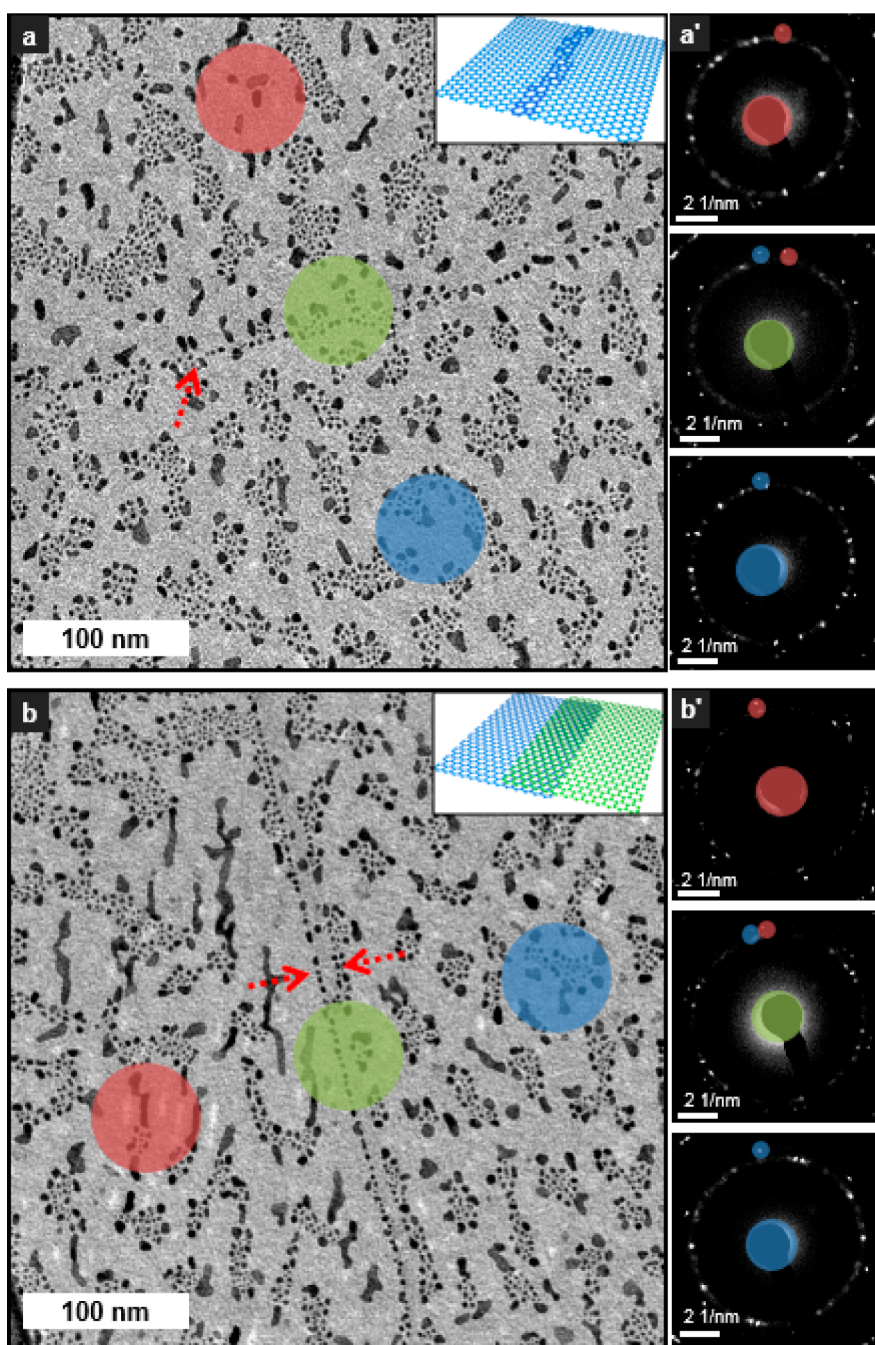
Figure 2. Correlation between a single line of gold NPs and grain boundaries. TEM images of gold NPs near stitched grain boundary (a) and overlapped grain boundary (b). Each colored SAED pattern is obtained from the same colored area in the TEM images (a′, b′). The insets in (a) and (b) represent a stitched grain boundary and overlapped grain boundary, respectively. The red arrows indicate GBs.

The inset of each figure in Figure 3 represents the corresponding structure of the wrinkles. To characterize the structure of the graphene surface at double lines of gold NPs, we observed the SEM image with tilting, which allows effective visualization of the three-dimensional landscape. Figure 3a and b are the SEM images without and with 60° tilting of double lines, respectively. Although it is unclear whether a double line represents a wrinkle in the top view, the narrow width and the shape of a wrinkle in Figure 3b clearly

indicate the presence of a standing collapsed wrinkle as previously reported.[7] Note that the width of a standing collapsed wrinkle is about 2 nm. As far as we know, the width scale of a standing collapsed wrinkle is the first reported. Typical AFM cannot exactly resolve the standing collapsed wrinkles because the width is below the lateral resolution. The aggregation of gold NPs as a wide line (Figure 3c) indicates the presence of a folded wrinkle. Figure 3d and Figure S4 represent the AFM topography of a folded wrinkle in
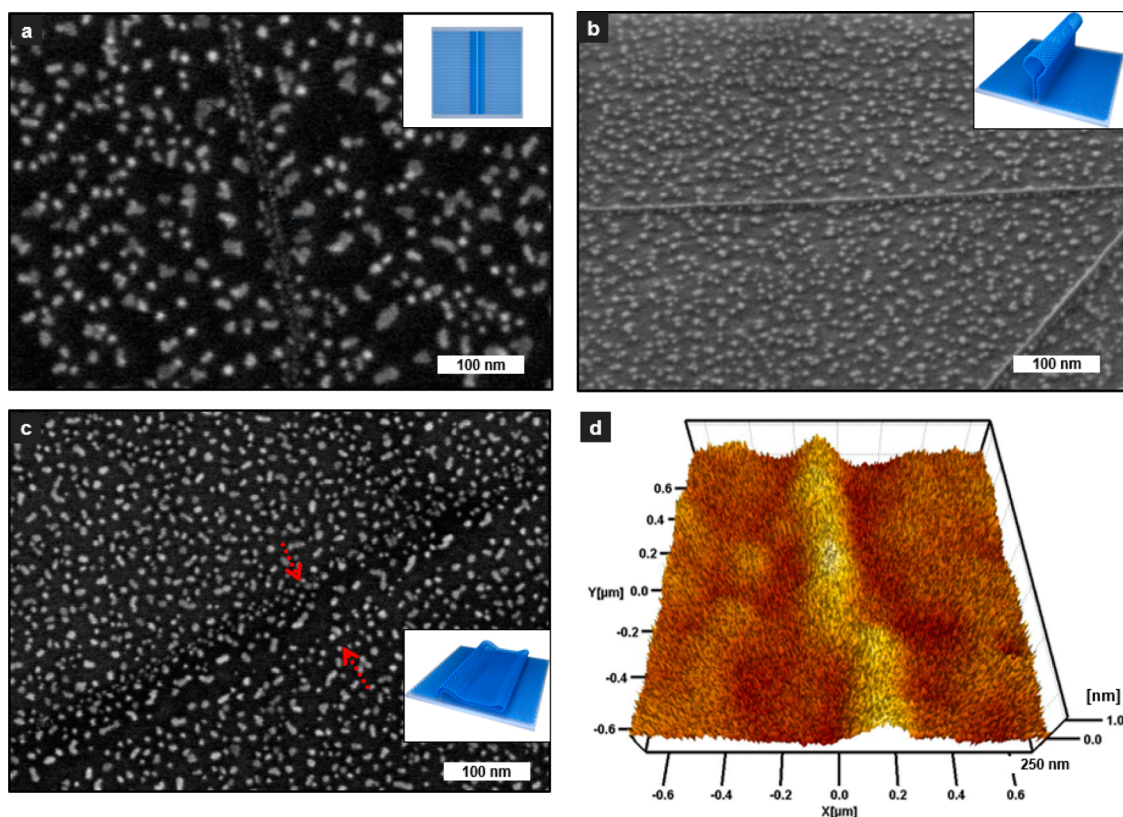
Figure 3. SEM images of a graphene wrinkle after gold deposition. SEM images without tilting of double lines (a) and with a 60° tilting of double lines (b). SEM images without tilting of wide lines (c) and AFM profile of a folded wrinkle (d). The insets of (a) and (b) represent the standing collapsed wrinkle, while those of (c) represent the folded wrinkle.
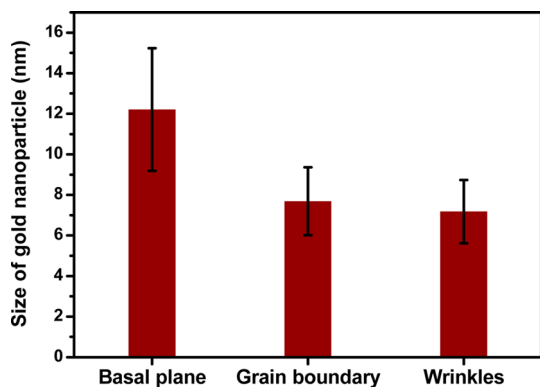

Figure 4. Size distributions of gold NPs on the graphene basal plane, GBs, and wrinkles. The average size of gold NPs near the basal plane, grain boundaries, and a wrinkle of graphene is 12.1 ± 1.5, 7.7 ± 1.7, and 7.1 ± 3 nm, respectively. A larger binding energy difference leads to a smaller diffusion coefficient and a smaller size of a gold NP.

agreement with Figure 3c and the previously reported data,[7] respectively.

We measured the size of gold NPs in Figure 1d. The size distributions of gold NPs show that line defects are the site providing a higher binding energy for gold clusters (Figure 4 and Figure S5). The average size of gold NPs on wrinkles, GBs, and the basal plane of graphene is 7.1, 7.7, and 12.1 nm, respectively. Gold NPs at line defects are generally smaller than those on

the basal plane of graphene. This could be explained by the growth mechanism consisting of three steps:[21] nucleation, diffusion-mediated growth, and adsorption-driven growth. When gold vapors contact the surface of graphene, they irregularly bounce laterally until they form a small cluster. This step is called nucleation. At the diffusion-mediated growth step, small clusters get larger by diffusion and coalescence of movable clusters in order to minimize the surface energy. In this step, the gold NPs exhibit a size difference at line defects and on the basal plane of graphene. The binding energy is the key microscopic quantity that determines the diffusion coefficient.[21] A larger binding energy difference can be correlated to a higher diffusion barrier, which in turn results in a smaller diffusion coefficient and a smaller threshold size of a gold NP. When a cluster becomes a certain threshold size, its mobility is dramatically reduced. After the threshold size, the growth of gold clusters is mainly dominated by adsorption-driven growth. In this step, adsorption of a moving adatom to an immobilized cluster is the main process for gold growth.

We found using first-principles calculations that line defects such as GBs and wrinkles provide a higher binding energy for gold adatoms. The computed models were a gold adatom on graphene, a graphene bilayer, a Stone–Wales defect of graphene, a glycolized Stone–Wales defect of graphene, an edge of a
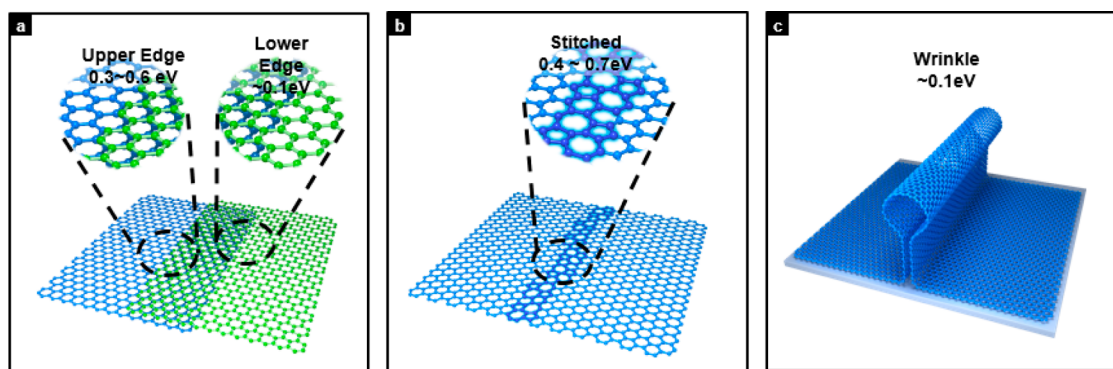
Figure 5. Relative binding energies (eV) of gold adatoms on three types of line defects with respect to those on pure graphene. The absolute binding energy of a gold adatom on pristine graphene is 0.4 eV, which is consistent with previously reported data.[22] When a gold adatom is on the upper/lower edge of an overlapped GB, its binding to the substrate is 0.3−0.6 eV/0.1 eV stronger than when it is on pristine graphene (a). The binding energies on stitched GBs are 0.4−0.7 eV higher (b), while those on wrinkles are ∼0.1 eV higher than those on the pristine graphene due to the enhanced sp^3 character (c).

graphene nanoribbon on graphene, and a hydroxylated edge of a graphene nanoribbon on graphene (Figure S6). Stone−Wales defects mimic stitched GBs (Figure 5a), while a graphene nanoribbon on graphene mimics the edge part of overlapped GBs (Figure 5b). We found that gold prefers to adhere to line defects even when there is no dangling bond. On a Stone−Wales defect, a gold adatom chemisorbs to the central double bond. In other cases, the charge transfer and consequent electrostatic interaction play a central role in increasing the binding energy. The gold adatom near an edge acquires a partial negative charge from neighboring carbon and hydrogen. The hydrogen acquires a partial positive charge from carbon and more from oxygen if it is nearby. The resulting charge−charge interaction constitutes most of the increased binding energy. To this end, an edge and a defect can easily accommodate immobile gold clusters, which attract other gold atoms or small gold clusters so that they grow.

On the other hand, the enhanced sp^3 character of carbons on a wrinkle and collision to a wrinkle lead gold NPs to agglomerate along wrinkles. The binding energy is increased due to the enhanced sp^3 character, as explained in the case of carbon nanotubes.[23] Additionally, a collision of a gold adatom with a wrinkle is expected to be inelastic, as if a nanobullet collides with a nano carbon net; that is, the gold adatom loses its kinetic energy as it collides. Such changes can facilitate agglomeration along wrinkles. When an edge is present under a pristine layer of graphene, this covered edge denotes the transition from single layer to bilayer. There is only a subtle difference in binding energy between a single layer and bilayer due to the van der Waals interaction and charge transfer. Therefore, the gold agglomeration along the covered edge is much weaker than that along the uncovered edge.

CONCLUSION

Gold deposition with careful control of annealing conditions achieves visualization of diverse surface structures of graphene. Grain boundaries and wrinkles are clearly visible as a single line and a double line of gold NPs under SEM. The TEM experiment directly proves that a single line of gold NPs corresponds to GBs, and the tilted-SEM images show that a double line of gold NPs corresponds to a wrinkle. The combined analysis of SEM and TEM images allows us to simultaneously inspect diverse line defect structures such as stitched GBs, overlapped GBs, standing collapsed wrinkles, and folded wrinkles. The observed pattern of gold NPs results from the fact that their diffusion is disrupted by line defects, providing abrupt changes in the binding energy, as proven by theoretical calculations. In addition, our method to simultaneously identify GBs and wrinkles does not require high-resolution TEM or STM. Our approach could also expand to other large-scale two-dimensional materials such as molybdenum disulfide and boron nitride by simply tuning annealing conditions.

METHODS

Synthesis of Graphene Using the CVD Process. Large-area graphene films were prepared by the CVD process using copper foil. Cu foil (99.999%, Alfa Aesar) was annealed at 1000 °C for 30 min under a hydrogen flow (8 sccm) to remove the metal oxide layer. While maintaining this temperature, methane gas was introduced at 24 sccm for 30 min at an operating pressure of 300 mTorr. After growth (methane flow), the sample was rapidly cooled to room temperature at a rate of 20 °C/min under the same hydrogen gas flow.

Transfer of Graphene to SiO$_2$/Si Substrate. After synthesis, as-grown graphene films on Cu foil were covered with poly(methyl methacrylate) (PMMA, M_w = 350 kg/mol^{-1}) and floated on a 0.1 M ammonium persulfate aqueous solution. After etching the Cu foil, the graphene with the PMMA support was transferred on the Si wafer with a 285 nm SiO$_2$ layer, and then the PMMA support was removed with acetone and additional thermal annealing.

Transfer of Graphene to a TEM Grid. We followed the procedure in ref 24. A holey carbon film on a 300 mesh gold grid was

wetted by isopropyl alcohol (IPA) and gently placed on top of as-grown graphene on Cu. The surface tension by evaporation of IPA induces a strong attractive force between graphene and the carbon film. After adhesion, the sample was floated on a 0.1 M ammonium persulfate aqueous solution to remove Cu contaminants.

Gold Evaporation on Graphene. Depositing gold and controlling the annealing condition were conducted using a thermal evaporator (DKOL04-02-T). Gold was purchased from Sigma-Aldrich (wire diameter 1.0 mm, 99.99%). Our experiment is reproducible; however, we found that the evaporation condition for the clearest visualization depends on the evaporation machine.

Characterization Techniques. SEM (Hitachi, S4800) was operated at 10 kV. TEM analyses were made with an image Cs-corrector electron microscope, JEM-2200FS, at an accelerating voltage of 200 kV. After transfer of graphene on the SiO_2 substrate, the Raman spectra were obtained with a Senterra Raman Scope system with a 532 nm wavelength incident laser light and a power of 20 mW.

Calculation Method. Spin-polarized plane-wave density functional theory calculations were performed by using VASP[25] 5.10 with standard PAW pseudopotentials. We used the optB88 functional[26] and cutoff of 500 eV. Ionic relaxation was done with a $3 \times 3 \times 1$ uniform k-points grid, and the single-point calculation was done with the $7 \times 7 \times 1$ grid, both including the gamma point. Because the unit cell was sufficiently large, the total energy converged with a relatively small number of k-points. A vacuum of longer than 10 Å and a dipole potential correction (with the corresponding energy correction) were applied to minimize spurious interactions between unit cells.

Conflict of Interest: The authors declare no competing financial interest.

Supporting Information Available: Additional experimental details. This material is available free of charge *via* the Internet at http://pubs.acs.org.

REFERENCES AND NOTES

1. Bae, S.; Kim, H.; Lee, Y.; Xu, X.; Park, J.-S.; Zheng, Y.; Balakrishnan, J.; Lei, T.; Ri Kim, H.; Song, Y. I.; *et al.* Roll-to-Roll Production of 30-in. Graphene Films for Transparent Electrodes. *Nat. Nanotechnol.* **2010**, *5*, 574–578.
2. Kim, K. S.; Zhao, Y.; Jang, H.; Lee, S. Y.; Kim, J. M.; Kim, K. S.; Ahn, J.-H.; Kim, P.; Choi, J.-Y.; Hong, B. H. Large-Scale Pattern Growth of Graphene Films for Stretchable Transparent Electrodes. *Nature* **2009**, *457*, 706–710.
3. Li, X.; Cai, W.; An, J.; Kim, S.; Nah, J.; Yang, D.; Piner, R.; Velamakanni, A.; Jung, I.; Tutuc, E.; *et al.* Large-Area Synthesis of High-Quality and Uniform Graphene Films on Copper Foils. *Science* **2009**, *324*, 1312–1314.
4. Huang, P. Y.; Ruiz-Vargas, C. S.; van der Zande, A. M.; Whitney, W. S.; Levendorf, M. P.; Kevek, J. W.; Garg, S.; Alden, J. S.; Hustedt, C. J.; Zhu, Y.; *et al.* Grains and Grain Boundaries in Single-Layer Graphene Atomic Patchwork Quilts. *Nature* **2011**, *469*, 389–392.
5. Kim, K.; Lee, Z.; Regan, W.; Kisielowski, C.; Crommie, M. F.; Zettl, A. Grain Boundary Mapping in Polycrystalline Graphene. *ACS Nano* **2011**, *5*, 2142–2146.
6. Yazyev, O. V.; Louie, S. G. Electronic Transport in Polycrystalline Graphene. *Nat. Mater.* **2010**, *9*, 806–809.
7. Zhu, W.; Low, T.; Perebeinos, V.; Bol, A. A.; Zhu, Y.; Yan, H.; Tersoff, J.; Avouris, P. Structure and Electronic Transport in Graphene Wrinkles. *Nano Lett.* **2012**, *12*, 3431–3436.
8. Song, H. S.; Li, S. L.; Miyazaki, H.; Sato, S.; Hayashi, K.; Yamada, A.; Yokoyama, N.; Tsukagoshi, K. Origin of the Relatively Low Transport Mobility of Graphene Grown through Chemical Vapor Deposition. *Sci. Rep.* **2012**, *2*.
9. Grantab, R.; Shenoy, V. B.; Ruoff, R. S. Anomalous Strength Characteristics of Tilt Grain Boundaries in Graphene. *Science* **2010**, *330*, 946–948.
10. Yu, Q.; Jauregui, L. A.; Wu, W.; Colby, R.; Tian, J.; Su, Z.; Cao, H.; Liu, Z.; Pandey, D.; Wei, D.; *et al.* Control and Characterization of Individual Grains and Grain Boundaries in Graphene Grown by Chemical Vapour Deposition. *Nat. Mater.* **2011**, *10*, 443–449.
11. Tsen, A. W.; Brown, L.; Levendorf, M. P.; Ghahari, F.; Huang, P. Y.; Havener, R. W.; Ruiz-Vargas, C. S.; Muller, D. A.; Kim, P.; Park, J. Tailoring Electrical Transport across Grain Boundaries in Polycrystalline Graphene. *Science* **2012**, *336*, 1143–1146.
12. Duong, D. L.; Han, G. H.; Lee, S. M.; Gunes, F.; Kim, E. S.; Kim, S. T.; Kim, H.; Ta, Q. H.; So, K. P.; Yoon, S. J.; *et al.* Probing Graphene Grain Boundaries with Optical Microscopy. *Nature* **2012**, *490*, 235–239.
13. Yu, S. U.; Cho, Y.; Park, B.; Kim, N.; Youn, I. S.; Son, M.; Kim, J. K.; Choi, H. C.; Kim, K. S. Fast Benchtop Visualization of Graphene Grain Boundaries Using Adhesive Properties of Defects. *Chem. Commun.* **2013**, *49*, 5474–5476.
14. Kim, D. W.; Kim, Y. H.; Jeong, H. S.; Jung, H.-T. Direct Visualization of Large-Area Graphene Domains and Boundaries by Optical Birefringency. *Nat. Nanotechnol.* **2012**, *7*, 29–34.
15. Fei, Z.; Rodin, A. S.; Gannett, W.; Dai, S.; Regan, W.; Wagner, M.; Liu, M. K.; McLeod, A. S.; Dominguez, G.; Thiemens, M.; *et al.* Electronic and Plasmonic Phenomena at Graphene Grain Boundaries. *Nat. Nanotechnol.* **2013**, *8*, 821–825.
16. Son, J.-H.; Baeck, S.-J.; Park, M.-H.; Lee, J.-B.; Yang, C.-W.; Song, J.-K.; Zin, W.-C.; Ahn, J.-H. Detection of Graphene Domains and Defects Using Liquid Crystals. *Nat. Commun.* **2014**, *5*.
17. Koepke, J. C.; Wood, J. D.; Estrada, D.; Ong, Z.-Y.; He, K. T.; Pop, E.; Lyding, J. W. Atomic-Scale Evidence for Potential Barriers and Strong Carrier Scattering at Graphene Grain Boundaries: A Scanning Tunneling Microscopy Study. *ACS Nano* **2012**, *7*, 75–86.
18. Zhou, H.; Qiu, C.; Liu, Z.; Yang, H.; Hu, L.; Liu, J.; Yang, H.; Gu, C.; Sun, L. Thickness-Dependent Morphologies of Gold on N-Layer Graphenes. *J. Am. Chem. Soc.* **2009**, *132*, 944–946.
19. Luo, Z.; Somers, L. A.; Dan, Y.; Ly, T.; Kybert, N. J.; Mele, E. J.; Johnson, A. T. C. Size-Selective Nanoparticle Growth on Few-Layer Graphene Films. *Nano Lett.* **2010**, *10*, 777–781.
20. Zhou, H.-q.; Yu, F.; Yang, H.-c.; Chen, M.-j.; Wang, G.; Sun, L.-f. High-Throughput Thickness Determination of N-Layer Graphenes *via* Gold Deposition. *Chem. Phys. Lett.* **2011**, *518*, 76–80.
21. Schwartzkopf, M.; Buffet, A.; Korstgens, V.; Metwalli, E.; Schlage, K.; Benecke, G.; Perlich, J.; Rawolle, M.; Rothkirch, A.; Heidmann, B.; *et al.* From Atoms to Layers: *In Situ* Gold Cluster Growth Kinetics during Sputter Deposition. *Nanoscale* **2013**, *5*, 5053–5062.
22. Lazar, P.; Zhang, S.; Šafářová, K.; Li, Q.; Froning, J. P.; Granatier, J.; Hobza, P.; Zbořil, R.; Besenbacher, F.; Dong, M.; *et al.* Quantification of the Interaction Forces between Metals and Graphene by Quantum Chemical Calculations and Dynamic Force Measurements under Ambient Conditions. *ACS Nano* **2013**, *7*, 1646–1651.
23. Durgun, E.; Dag, S.; Bagci, V. M. K.; Gülseren, O.; Yildirim, T.; Ciraci, S. Systematic Study of Adsorption of Single Atoms on a Carbon Nanotube. *Phys. Rev. B* **2003**, *67*, 201401.
24. Regan, W.; Alem, N.; Alemán, B.; Geng, B.; Girit, Ç.; Maserati, L.; Wang, F.; Crommie, M.; Zettl, A. A Direct Transfer of Layer-Area Graphene. *Appl. Phys. Lett.* **2010**, *96*, 113102.
25. Kresse, G.; Furthmüller, J. Efficiency of *Ab-Initio* Total Energy Calculations for Metals and Semiconductors Using a Plane-Wave Basis Set. *Comput. Mater. Sci.* **1996**, *6*, 15–50.
26. Jiří, K.; David, R. B.; Angelos, M. Chemical Accuracy for the Van der Waals Density Functional. *J. Phys.: Condens. Matter.* **2010**, *22*, 022201.